remote sensing

MDPI

Article

Assessment and Validation of FAPAR, a Satellite-Based Plant Health and Water Stress Indicator, over Uganda

Ronald Ssembajwe [1,2], Amina Twah [1], Godfrey H. Kagezi [2], Tuula Löytty [3], Judith Kobusinge [2], Anthony Gidudu [4], Geoffrey Arinaitwe [2], Qingyun Du [5] and Mihai Voda [6,*]

[1] College of Agricultural and Environmental Sciences, Makerere University, University Rd, Kampala P.O. Box 7062, Uganda; ronald.ssembajwe@students.mak.ac.ug (R.S.); twah.amina@students.mak.ac.ug (A.T.)
[2] National Coffee Research Institute, National Agricultural Research Organization, Mukono P.O. Box 185, Uganda; godfrey.kagezi@naro.go.ug (G.H.K.); judithkobusinge25@gmail.com (J.K.); director.nacorri@naro.go.ug (G.A.)
[3] Smart & Lean Hub Oy (S&L), Luumukatu 4, 15320 Lahti, Finland; tuula.loytty@smartlean.fi
[4] College of Engineering, Design Art and Technology, Makerere University, University Rd, Kampala P.O. Box 7062, Uganda; anthony.gidudu@mak.ac.ug
[5] School of Resource and Environmental Sciences, Wuhan University, 129 Luoyu Road, Wuhan 430079, China; qydu@whu.edu.cn
[6] Faculty of Geography, Dimitrie Cantemir University, Bodoni Sándor Street 3–5, 504545 Târgu Mureș, Romania
* Correspondence: mihaivoda@cantemir.ro

Highlights

What are the main findings?

- Monthly photosynthetic activity (FAPAR) over Uganda has been increasing, becoming highly variable and dominated by a moderate activity of 0.35–0.45 units.
- The Standardized FAPAR Index (SFI) had strong positive and negative correlations with the scale 3 Standardized Precipitation and Evapotranspiration Index (SPEI-03) and crop water stress index (CWSI), respectively.

What are the implication of the main findings?

- The observed distribution and patterns of photosynthetic activity are jointly governed by precipitation, evapotranspiration, LULC, and teleconnections.
- Satellite-based FAPAR products can suitably track ecosystem functionality over Uganda, with an emphasis on water stress.

Abstract

This study aimed to assess, compare, and validate a satellite-based plant health and water stress indicator: Fraction of Absorbed Photosynthetically Active Radiation (FAPAR) over Uganda. We used a direct agricultural drought indicator—the Standardized Precipitation and Evapotranspiration Index at scale 3 (SPEI-03)—and a plant water stress indicator—the crop water stress index (CWSI)—for the period of 1983–2013. Novel approaches such as spatial variability and trend analysis, along with correlation analysis, were used to achieve this. The results showed that there are six classes of highly variable photosynthetic activity over Uganda, dominated by class 4 (0.36–0.45). This dominant class encompassed 45% of the total land area, mainly spanning cropland. In addition, significant increases in monthly photosynthetic activity (FAPAR) and FAPAR-centered stress indicators (SFI < −1) were observed over 85% and 60% of total land area, respectively. The Standardized FAPAR Index (SFI) had a strong positive correlation with SPEI-03 over cropland, grassland, and forest lands, while SFI had a strong negative correlation with CWSI over 80% of the total area. These results highlight the state and variation in plant health and water stress,

check for updates

Academic Editors: Fei Zhang, Xiaoping Wang, Brian Alan Johnson and Xu Ma

Received: 22 July 2025
Revised: 24 September 2025
Accepted: 25 September 2025
Published: 21 October 2025

Citation: Ssembajwe, R.; Twah, A.; Kagezi, G.H.; Löytty, T.; Kobusinge, J.; Gidudu, A.; Arinaitwe, G.; Du, Q.; Voda, M. Assessment and Validation of FAPAR, a Satellite-Based Plant Health and Water Stress Indicator, over Uganda. *Remote Sens.* **2025**, *17*, 3501. https://doi.org/10.3390/rs17203501

Copyright: © 2025 by the authors. Licensee MDPI, Basel, Switzerland. This article is an open access article distributed under the terms and conditions of the Creative Commons Attribution (CC BY) license (https://creativecommons.org/licenses/by/4.0/).

generate insights on ecosystem dynamics and functionality, and weigh in on the usability and reliability of satellite-based variables such as FAPAR in plant water monitoring over Uganda. We thus recommend satellite-based FAPAR as a robust proxy for vegetation health and water stress monitoring over Uganda, with potential application in crop yield prediction and irrigation management to inform effective agricultural planning and improve productivity.

Keywords: FAPAR; satellite-based; plant water stress; photosynthetic activity; SPEI; trends; validation; Uganda

1. Introduction

Droughts continue to prevail as the most frequent and costly natural disasters on Earth. Remotely sensed biophysical variables such as fraction of absorbed photosynthetically active radiation (FAPAR) have previously garnered global credit in assessing plant health with emphasis on photosynthetic activity and plant water stress. FAPAR is the fraction of incoming solar radiation in the spectrum of 400–700 nm that is absorbed by the vegetation canopy, and it is a ratio that ranges from 0 to 1, with no units [1]. Radiation in this spectrum can be used by the vegetation canopy in photosynthesis with a unit of measurement of $\mu molm^{-2}s^{-1}$ [2,3]. Vegetation photosynthesis is responsible for the conversion of about 50 PgC/yr1 of atmospheric CO_2 into biomass, which represents about 10% of the atmospheric carbon content [3]. FAPAR is also a key indicator of vegetative water [4] and energy balance, and it is also an important parameter in ecosystem models, climate models, vegetation net primary productivity (NPP) estimation models, and crop yield estimation models [5]. For example, a 10% increase in FAPAR would result in equal amounts of Gross Primary Product (GPP) [6], NPP, and carbon sink increases [3]. FAPAR is one of the 50 essential climate variables recognized by the UN Global Climate Observing System [7]. Intrinsically understanding the magnitude and changes in FAPAR provides critical information on both the productivity and efficiency of plant canopies and ecosystems, respectively. In Uganda, in spite of its core importance, studies on the evolution of FAPAR are insufficient. That is, only one research has been identified which explores PAR in the Manafwa catchment in Mt. Elgon region; moreover, this study only analyzed a short period of time. In their research, Oyana et al. [8] reported significant spatial and temporal differences in Leaf Area Index (LAI) and PAR over the study area.

FAPAR can be estimated by both ground-based and space-based approaches from vegetation indices such NDVI and LAI, among others. Ground-based estimates of FAPAR require the simultaneous measurement of PAR above and below the canopy [9], while space-based approaches involve retrieval of vegetation indices from space remote sensing platforms using physically based inverse methods. Both ground-based and space-based approaches and numerical methods for FAPAR estimation have been summarized by Liang et al. [3]. Today, the evolution of space-based observation technologies has presented both opportunities and challenges to researchers for further exploration of the Atmosphere–Lithosphere–Biosphere continuum. For a variety of uses, numerous satellite-based worldwide FAPAR datasets have been created and are regularly updated. The Joint Research Center (JRC) FAPAR, Sentinel-3, Advanced Very High-Resolution Radiometer (AVHRR), Satellite Pour l'Observation de la Terre VÉGÉTATION (SPOT-VEGETATION), Moderate Resolution Imaging Spectroradiometer (MODIS), and others are among these FAPAR datasets. Of these, several datasets including GEOV2 FAPAR, MODIS FAPAR, and

AVHRR-based FAPAR [2] have been harmonized with continuous improvement in both temporal and spatial resolutions as well the quality aspects [10].

In this study, AVHRR-based FAPAR was chosen for its consistency; continuity when extended over long periods; validity, characterized by few errors [11]; ability to reproduce ecosystem dynamics and annual cycles over the tropics [10]; and its ready-to-use and high temporal resolution attributes. The National Oceanic and Atmospheric Administration's Climate Data Record (NOAA-CDR), also known as AVH15C1, is the longest, most consistently calibrated, and atmospherically corrected FAPAR [10]. The dataset is derived from AVHRR's carefully calibrated and corrected land surface reflectance dataset (AVH09C1), combining existing FAPAR datasets such as MODIS FAPAR (MCD15A2) as well as NDVI relationships as a backup using Artificial Neural Networks. AVH15C1 is calibrated and validated using the BELMANIP2 network and the DIRECT network, respectively. A detailed description of the AVH15C1 derivation can be found in Claverie et al. [11].

Despite the fact that FAPAR products including AVH15C1 have had extensive validation and several applications such as drought monitoring, studies have noted discrepancies and inconsistencies within the datasets. Furthermore, questions on efficient applicability of FAPAR in plant water stress monitoring remain unanswered in sub-Saharan Africa, especially Uganda. Therefore, this study aims to achieve the following:

(i) Explore the spatiotemporal variability of FAPAR of Uganda;
(ii) Determine trends in FAPAR and FAPAR-centered stress indices (SFI > −1);
(iii) Compare and indirectly validate FAPAR using the Standardized Precipitation and Evapotranspiration Index at scale 3 (SPEI-03) and crop water stress index (CWSI) over Uganda at high spatial resolutions to facilitate their smooth adoption in Uganda.

This study adopts similar approaches with Peng et al. [12] over Australia. However, we extend our analysis with more direct plant stress indices such as CWSI to assess and validate FAPAR over Uganda.

2. Description of Study Area

This study focuses on Uganda (Figure 1: Taken from Ssembajwe et al. [13]), a developing tropical country found in East Africa [14] situated within 1°S–5°N and 29°E–36°E [15,16]. The area is generally low lying in the L. Victoria and Kyoga basins with a gradual slope reducing towards the West Nile stretch. The average altitude in Lake Victoria Basin and West Nile is 1100 m and 900 m, respectively, while the western and southwestern regions such as the Mt Rwenzori slopes, Kigezi sub-region, Isingiro, and eastern regions of Mt Elgon are generally mountainous with average altitudes of 1800 m and above [17].

The region is dominated by an equatorial type of climate with two distinct (bimodal) wet seasons [14]. These are mainly experienced in the eastern, western and central parts between February and May and September to December, while the northern sub-region has a unimodal rainfall pattern, mainly concentrated between April and July. The mean monthly rainfall ranges from >250 mm over the shores of L. Victoria and highland areas to <50 mm over north east part of Uganda, Karamoja [18]. The main rains are received between March and June. Rainfall totals of more than 500 mm during this season typically provide enough water for crops and livestock [19]. Approximately 44 percent of Uganda's land area is under agriculture with 99 percent of it under subsistence agriculture [20]. Grasslands cover 23 percent of the land area. Figure 2, from Karamage et al. [20], shows Uganda's land use and land cover in 2016.

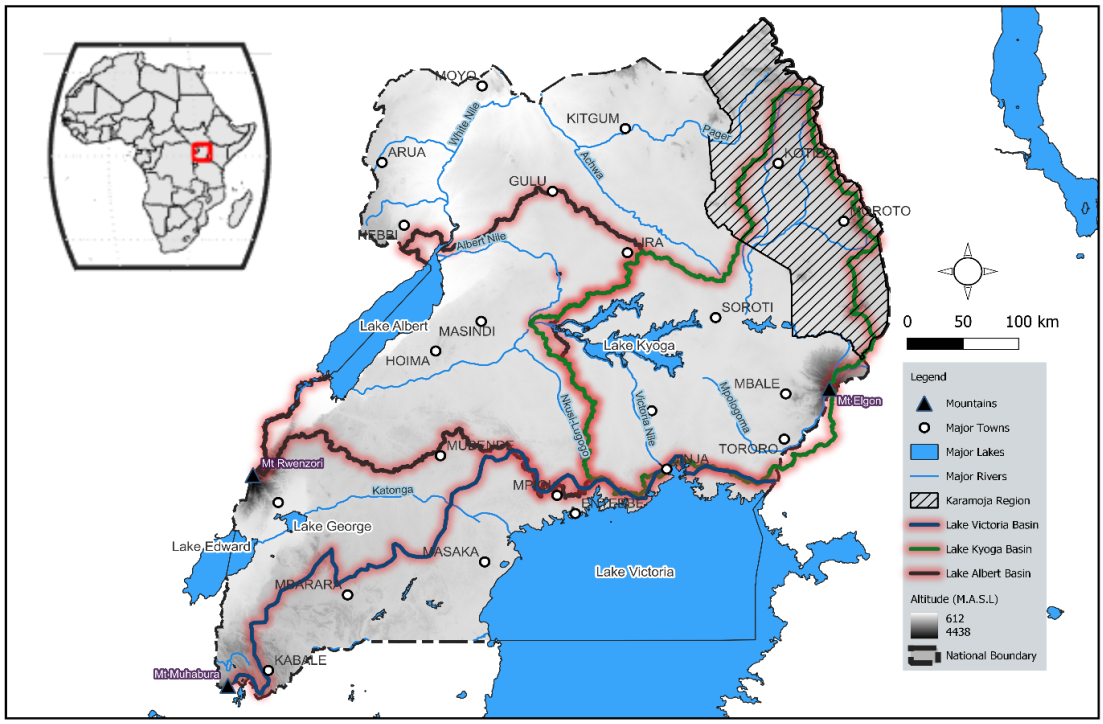

Figure 1. Location of Uganda on the African continent (red square), its topo-hydrography, and major towns and regions.

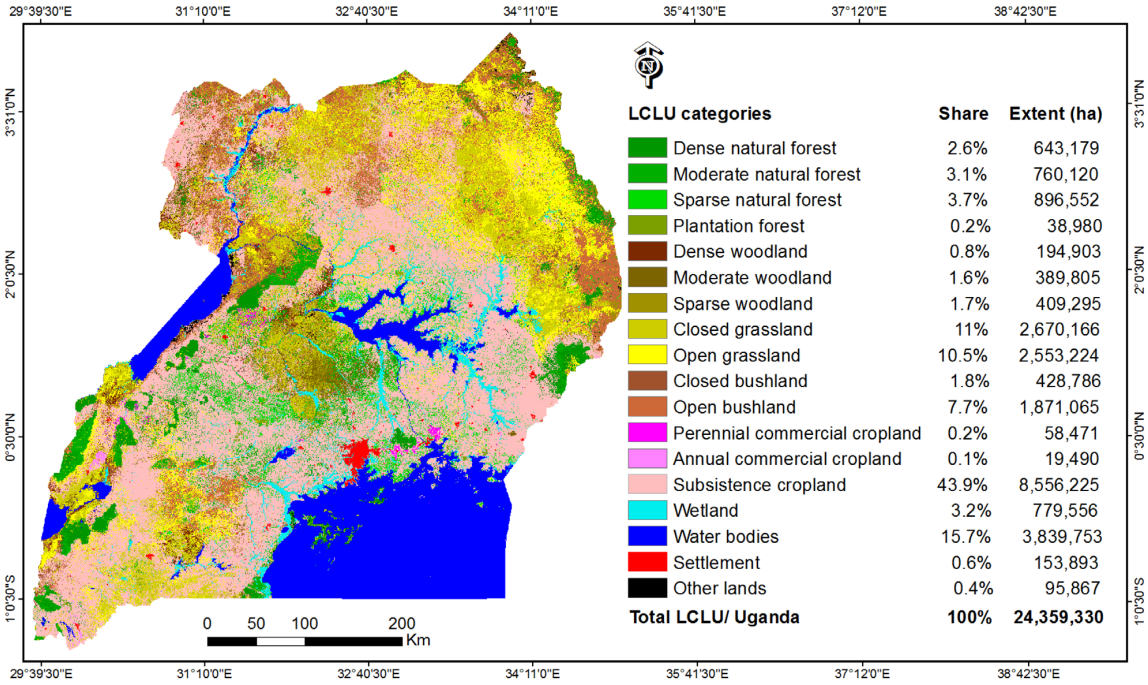

Figure 2. Uganda LULC classes at 30 m resolution based on LULC-2014 data [21].

3. Data and Methods

In this study, high spatial resolution biophysical and agroclimatic datasets such as FAPAR [11], precipitation, and actual and potential evapotranspiration data [22] for SPEI-03 and CWSI computation were sourced. This data was subjected to preprocessing. FAPAR data was used to compute the Standardized FAPAR Index (SFI) at a one-month scale. Both FAPAR and FAPAR-centered stress (SFI < -1) climatology and trends were computed. Later, SFI was compared with SPEI-03 indices and CWSI using correlation metrics.

3.1. Data Sources and Preprocessing

3.1.1. Data Acquisition

Daily FAPAR (AVH15C1) at ~5 km resolution was sourced from NOAA-CDR [11] in Network Common Data Form (NetCDF) format. The data was read in a MATLAB software [23] environment using ncdisp and ncread functions. While the data had no quality flags owing to its ready-to-use attribute, we subjected it to completeness and quality checks using isnan function and logical operators, respectively. The completeness test returned a negligible missing rate of 0.58% while the validity check (defined as 0–1 range for FAPAR) returned no values out of range. Furthermore, we used the 3-sigma rule [24] to check for outliers in the standardized FAPAR dataset (later defined as Standardized FAPAR Index). The test equally returned an outlier rate of 0%. FAPAR was later time-averaged to monthly temporal resolution using MATLAB scripts. The process involves binning daily FAPAR into annual and monthly cycles based on the time/datetime vector corresponding to the FAPAR dataset using the unique function in MATLAB. The outputs are then reshaped to the original dimensions and averaged based on a given month's length via a for loop. The output is then saved as Monthly FAPAR data. Monthly FAPAR was further aggregated into four main seasons, namely the following: December–February (DJF), March–May (MAM), June–August (JJA), and September–November (SON) using the monthly function in the CDT toolbox version 1 [25].

Monthly precipitation and evapotranspiration data for both potential and actual evapotranspiration at ~4 km were obtained from TerraClimate [22], also in NetCDF format. The TerraClimate database is a high-resolution (~4 km) global climate dataset that provides monthly climate and climatic water balance information for terrestrial surfaces (from 1958 to present) [13]. TerraClimate was chosen for its consistency, higher spatial resolution, and ability to reproduce the local climatology of Uganda [18]. These ancillary climate variables were equally read into a MATLAB environment and subjected to equal quality tests. All datasets can be obtained in the Supplementary Materials.

All datasets were then masked to country polygon shapes based on Uganda administration vectors using the mask function in MATLAB. Precipitation and evapotranspiration data were upscaled to match the ~5 km FAPAR spatial resolution, respectively. The conservative second-order remapping method [26,27] was used to remap the datasets with the help of Climate Data Operator (CDO) software [28] command lines. The CDO command line for remapping a given .nc file A based on the grid spacing of a .nc file B is given as follows:

cdo remapcon,B.nc A.nc NewA.nc.

3.1.2. Computation of Standardized FAPAR Index (SFI), Scale-03 Standardized Precipitation and Evapotranspiration Index (SPEI-03), and Crop Water Stress Index (CWSI)

A variety of indices using meteorological, hydrological, and agricultural data or a combination of all have been used to quantify droughts [29] and or water stress owing to a prolonged water deficit. The widely used technique is the z-scores method to standardize anomalies of a given agro- or hydrometeorological variable X [29–31]. In this study, FAPAR anomalies were standardized using a one-month interval. The Standardized FAPAR Index (SFI) based on Peng et al. [12] was thus given as follows:

$$SFI_{i,j} = \frac{FAPAR_{i,j} - \overline{FAPAR}_j}{\partial_j} \quad (1)$$

where i is the observation year from 1983 to 2013, j is the observation month from January to December, and $\overline{FAPAR}_j$ and ∂_j are the average and standard deviation of FAPAR in month j, respectively. FAPAR water stress was defined as SFI < −1.

The Standardized Precipitation and Evapotranspiration Index is a multiscalar drought index based on water balance between precipitation and potential evapotranspiration [32].

The index was developed by Vicente-Serrano in 2009 to help account for the temperature effects of global warming on the hydrological cycle. It has since been adopted in several hydrological, meteorological, and agroclimatic studies to quantify droughts. Thus, we computed a 3-month lagged SPEI in this study to account for delayed vegetation response to water stress following the approach by Vicente-Serrano et al. [32]. That is, a 3-month SPEI at the end of February compares the December–January–February water balance total in that particular year with the December–February water balance totals of all the years on record for that location [33]. First, we computed the climate water balance (D) as follows:

$$D_{i,j} = P_{i,j} - PET_{i,j} \quad (2)$$

where P_i is the precipitation during month j in the year i of a given grid cell, PET_i is the potential evapotranspiration during month j in the year i of a given grid cell. We then aggregated the $D_{i,j}$ series over a 3-month period as a moving sum. This was followed by fitting a logistic distribution to the aggregated D series. We then computed the cumulative distribution function (cdf) of the new probability distribution. Finally, we standardized the raw water balance cdf to obtain the SPEI-03 indices. A detailed overview of the SPEI computation procedure can be found in Vicente-Serrano et al. [32].

The crop water stress index was computed based on Jackson et al. [34] as follows:

$$CWSI = 1 - \frac{E_a}{E_p} \quad (3)$$

where E_a is the actual evapotranspiration in mm and E_p is the potential evapotranspiration in mm. CWSI is thus dimensionless and takes a range of 0 to 1, with lower values indicating no water stress or well water vegetation and higher values indicating water stress.

Table 1 shows the summary of data and its sources.

Table 1. Data and sources.

Variable	Temporal	Spatial	Period	Notes	Reference
FAPAR	Daily	~5 km	1983–2013	Directly sourced from NOAA-CDR	[11]
SPEI-03	Monthly	~4 km	1983–2013	Computed from precipitation and potential evapotranspiration data	[22,34]
CWSI	Monthly	~4 km	1983–2013	Computed from actual and potential evapotranspiration data	[22,34]

3.2. Data Analysis

3.2.1. Climatology and Variability Analysis

We started by computing the long-term spatiotemporal means of monthly and seasonal aggregated FAPAR using the statistical and geospatial techniques such as k-Means clustering [35], embedded in the mapping tool box and implemented in MATLAB R2024a [23]. We then computed the spatiotemporal variability of FAPAR as a variance at a given grid cell across the four main seasons over the study period. This variance, also given as the square of standard deviation of each of the climate variables, was then expressed as contours using the contour function embedded in the CDT Toolbox version 1 [25] in MATLAB R2024a. Variability analysis was chosen as it helps to reveal the instability of a given climate variable in space and time [13].

3.2.2. Non-Parametric Statistical Test for Trends in FAPAR and FAPAR-Centered Stress (SFI < −1)

In order to analyze long-term temporal and spatial trends, the modified Mann–Kendall trend test and Sen's slope estimator (MKSSE) were used. The Mann–Kendall test is a

statistical test widely used for the analysis of trend in climatologic and in thermal and hydrometeorological time series [36] such as temperature, rainfall, evaporation, evapotranspiration, streamflow, and water quality [37]. There are two advantages of using this test. First, it is a non-parametric test and does not require the data to be normally distributed. Second, the test has low sensitivity to abrupt breaks due to inhomogeneous time series [38]. According to this test, the null hypothesis H_o assumes that there is no trend (the data is independent and randomly ordered) and this is tested against the alternative hypothesis H_1, which assumes that there is a trend. The Z statistic is used to evaluate a trend; a positive (negative) value of Z means an increasing (decreasing) trend [39].

It follows that, from the hypothesis, that there no trend is rejected when the Z value is greater in absolute value than the critical value at a chosen level of significance (α); for example, in this study, this is $\alpha = 0.95$. In the Mann–Kendall test, the null hypotheses were tested at 95% confidence level for FAPAR and SFI < -1 trends and their respective magnitudes using the non-parametric Sen's slope. The test was implemented in MATLAB using the ktaub function [40] for computing the Mann–Kendall trend test and Sen's slope [25]. The function features Fisher's Z-Transformation for confidence limits for uncertainty quantification [41]. The results were mapped in MATLABR2024a using the pcolor function and based on a linear interpolation algorithm.

3.2.3. Spatiotemporal Correlation Analysis

Correlation coefficients are widely used to measure association between variables measured across a set of spatial locations in time. Thus, it is a strong performance metric used in comparison and validation studies across remote sensing and digital image processing disciplines. In this study, we computed the Pearson correlation coefficient between the SFI and SPEI-03 per pixel [42] using the Corr function in MATLAB R2024a via nested loop as an attempt to indirectly validate the satellite-based plant health and water stress indicator (FAPAR). This approach was chosen for its robustness as it ensures grid independence and seamless performance. The significance of the association was tested at $\alpha = 0.05$ level of significance. A similar procedure was repeated for ascertaining the relationship between SFI and CWSI. We quantified the uncertainty of the correlation coefficient (r) using Fisher's Z-Transformation for confidence limits [41]. The results were equally visualized using pcolor function in MATLAB R2024a.

Figure 3 shows the research design and flow process adopted for this study.

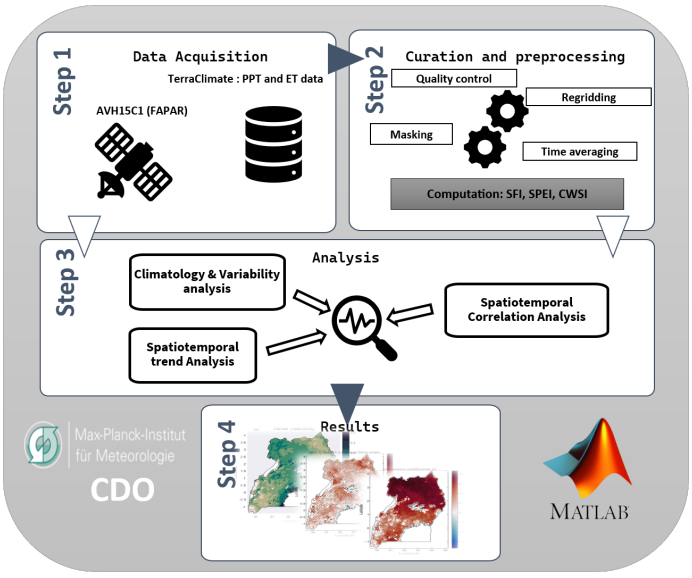

Figure 3. Graphical overview of the methodology for the study.

4. Results

4.1. FAPAR Climatology over Uganda (1983–2013)

Uganda's photosynthetic activity for the period (1983–2013) can be summarized in six homogenous classes represented by six shades of green: blumine, sage green, dusty green, light sage, pale hearth, and pale white (Figure 4). Class 1 (pale white) with the lowest photosynthetic activity of <0.18 FAPAR covers 8% of the total land area, mainly comprising highland areas. Class 2 (pale hearth) follows with the second lowest FAPAR in the range of 0.18–0.27. It occupies 13% of the country, covering areas like the Mt Elgon slopes, mid Karamoja, and southwestern Uganda. Class 3 (light sage) has an 18% coverage. The class assumes an eastern diagonal S.E to north stretch spanning the Mbale–Soroti districts to Kitgum district in the north and a western extension covering parts of central, western, southern, and northern Uganda. FAPAR in Class 3 ranged from 0.27 to 0.36. Class 4 (dusty green) dominated the country with moderate photosynthetic activity in the range of 0.36–0.45, covering 47% of the total land area. It comprises a diagonal L. Victoria–West Nile stretch, spanning the western and eastern L. Kyoga and L. Albert basins, respectively, to the northwestern (West Nile) region. Class 5 (sage green) had the second highest photosynthetic activity, covering up to 10% of the total land area. The class mainly centers around lakes Victoria and Kyoga with a pronounced 60 km buffer from L. Victoria. It also surrounds the White Nile in the northwest and a cluttered distribution over the western Uganda. FAPAR in this class ranged from 0.45 to 0.54. Finally, Class 6 (blumine) with the highest FAPAR over Uganda had the smallest coverage of 4%, mainly confined within the Lake Victoria shores. It is buffered by Class 5 on the outside, with a 0.54–0.8 FAPAR range.

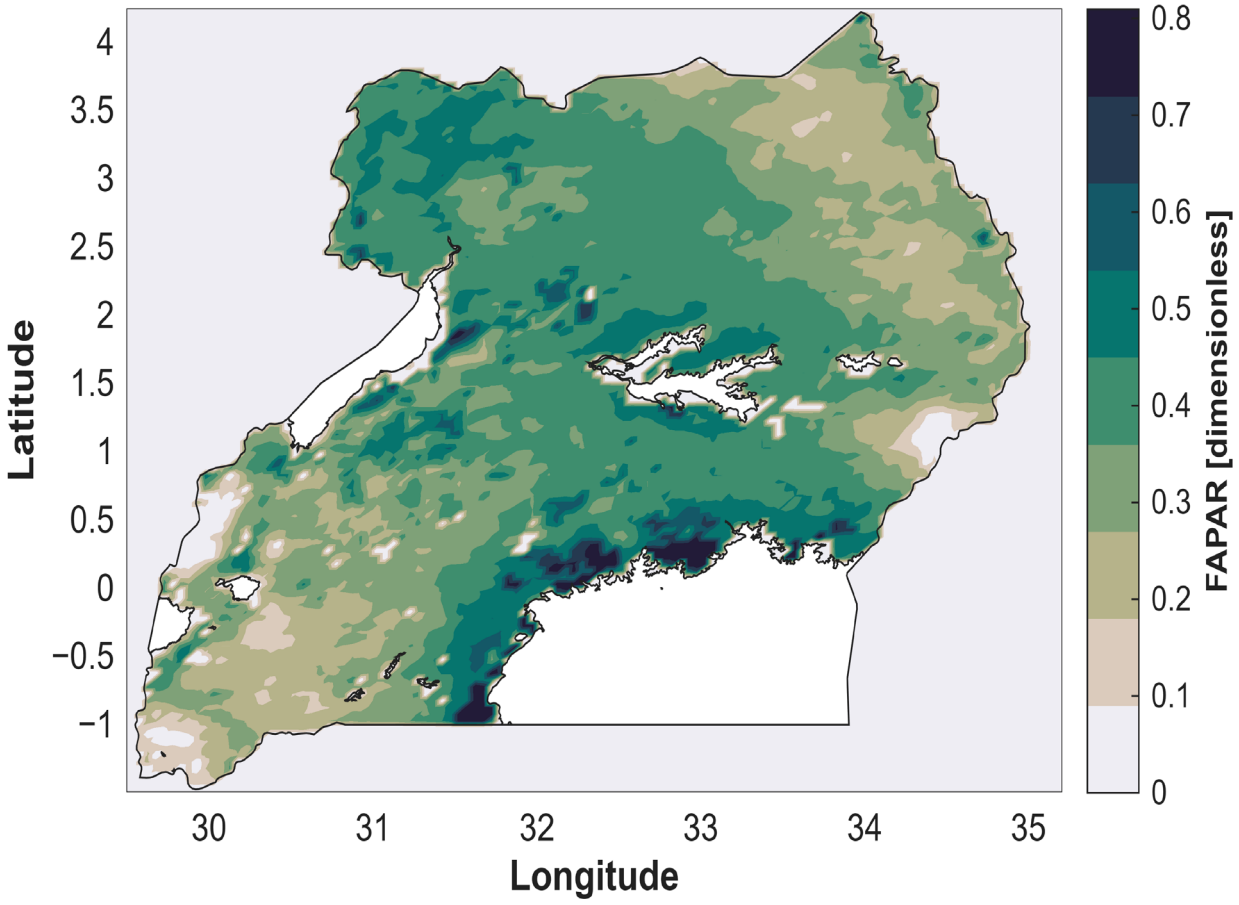

Figure 4. Monthly climatology of FAPAR over Uganda (1983–2013).

On the other hand, the monthly climatology of SFI < −1 (Figure 5) revealed dominance of mild FAPAR stress during the period 1983–2013. That is, 60% of the total land area was dominated by a FAPAR deficit in the range −1.4 to −1 encompassing the Greater Ankole-Masaka region, the L. Kyoga Basin, the districts between Jinja and Soroti, and the north–northwestern stretch. This was followed by moderate FAPAR deficit in the range −2 to −1.5 over the greater Karamoja region, the Mid-West Nile, as well as areas of Mubende in central Uganda, corresponding to 15%. Strong FAPAR anomalies below −2 were observed in Mt. Elgon, Rwenzori, Mbarara–Masaka–Kabarole transition, and along the Victoria Nile corresponding to 10% of the total land area. On the other hand, areas surrounding L. Victoria, the southeast of L. Kyoga, the western side of L. Albert, Kyenjojo, Hoima, Bushenyi, and the Kibale–Kabalore stretch were not associated with negative FAPAR anomalies.

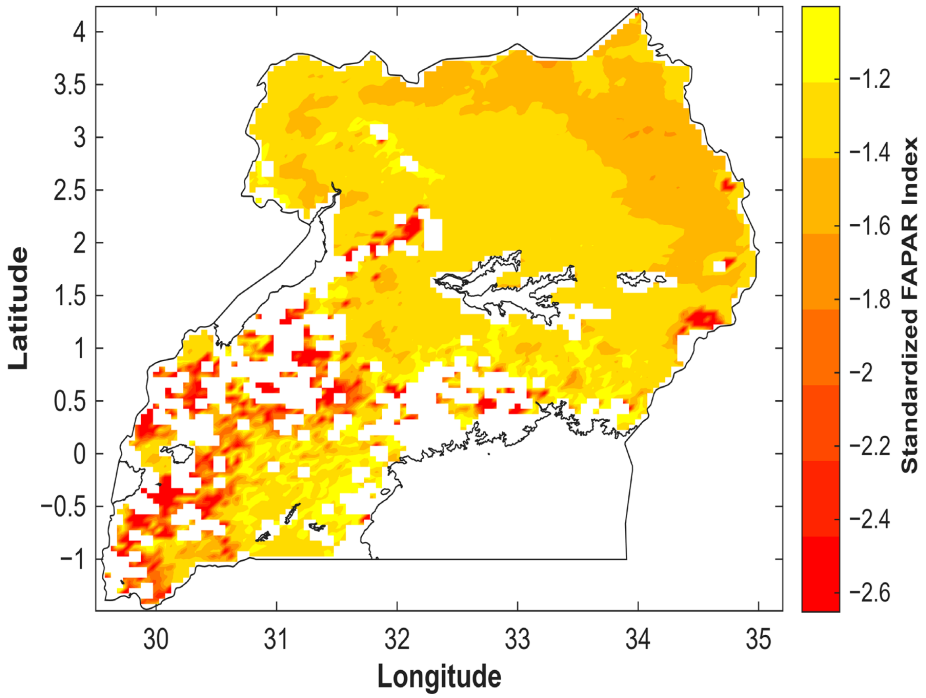

Figure 5. Monthly climatology of FAPAR-centered stress (SFI < −1) over Uganda (1983–2013).

At a seasonal level (Figure 6), photosynthetic activity varied significantly in both space and time. For example, during the dry DJF season, Karamoja, West Nile, and the south-western regions of Uganda were dominated by low but relatively stable photosynthetic activity in the range of 0.1–0.03. Contrarily, the central and western regions were dominated by higher FAPAR in the range of 0.4–0.6 characterized with high variability during this season. A gradual increase in FAPAR with a northward extension was observed during the wet MAM season over the central north and the West Nile regions. The extension is also characterized with an increase in FAPAR's temporal variability during this time of the year. However, the western and southwestern parts of the country experienced reductions in FAPAR characterized with increased variability. The lowest photosynthetic over the country was observed during the JJA season, where, aside from the L. Victoria buffer and West Nile, the country experienced FAPAR below 0.4, with extremes over the Mbale–Karamoja stretch and the Mubende–Masaka–Mbarara–Kabale to the Rwenzori stretch. During SON, the activity increased over the central, Kyoga, north, and northwestern regions of the country. SON was also the season when highest vegetation performance coverage over the country was recorded in the areas listed above. However, low activity was still recorded for southwestern and northeastern parts of the country during this time.

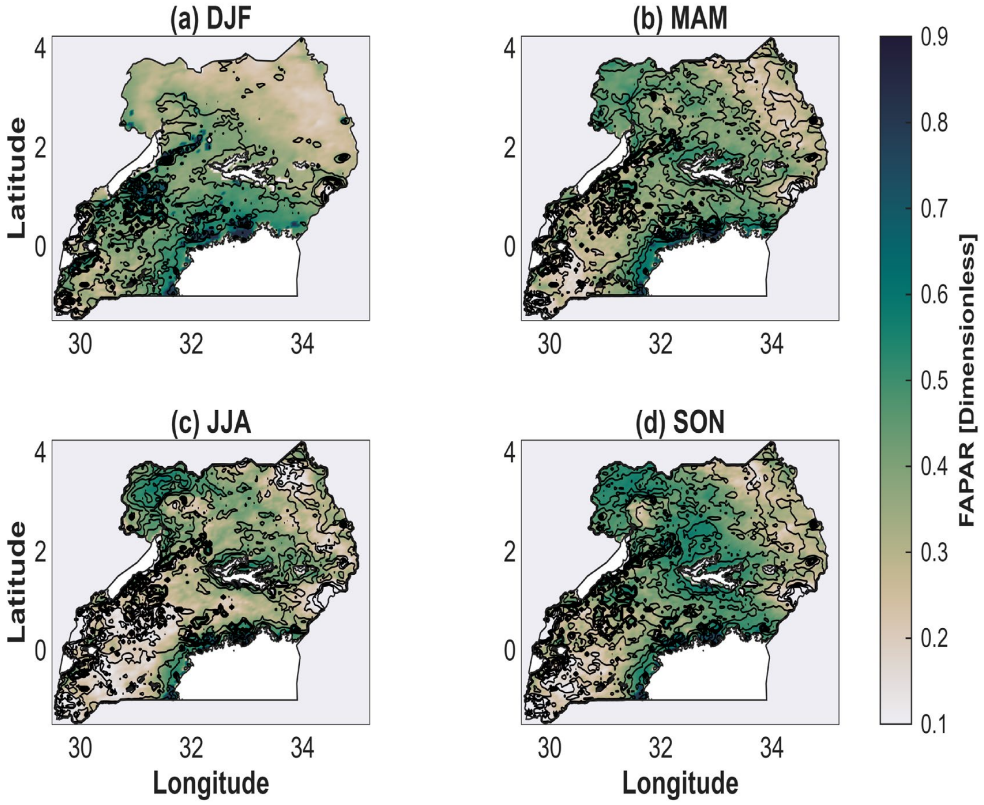

Figure 6. Seasonal climatology of FAPAR for the four main seasons: (**a**) December–February, (**b**) March–May, (**c**) June–August and (**d**) September–November and their variability (expressed as black contours) over Uganda (1983–2013).

4.2. Trend in FAPAR and FAPAR-Centered Stress Indices (SFI < −1) over Uganda (1983–2013)

The trend in monthly FAPAR (Figure 7) was dominated by increases for the study period spanning over 85% of the total land area. The strongest trend magnitudes were observed in Mbale, the slopes of Mt. Rwenzori in southwestern Uganda, the Albert Nile region in the northwest, and the River Pager basin in northeastern Uganda at a mean magnitude of 1.8×10^{-5} per month with a 95% confidence limit of 7.5×10^{-6} to 2×10^{-5} per month at a 5% level of significance. This was followed by the areas of the central West Nile, the Mubende–Masindi–Nakasongola triangle in the southern Lake Albert Basin, and the Mbarara–Sembabule stretch, with a mean magnitude of 1×10^{-5} per month in the range of 5×10^{-6} to 1.5×10^{-5}. The lowest positive magnitudes of the trend were observed in the Gulu–Kitgum stretch over northern Uganda, the western tips of the West Nile region, the Jinja–Tororo–Soroti stretch in eastern Uganda, and areas within the Lake Victoria Basin at $<5 \times 10^{-6}$ per month. Only a negligible 5% of the total land area had decreasing photosynthetic activity at -1×10^{-5} per month. This is observed in urban areas such as the Greater Kampala Metropolitan Area, Entebbe, the Mt. Elgon peaks, and areas within a 10 km radius of Lake Victoria.

Similarly, FAPAR-centered stresses (SFI < −1) (Figure 8) had a fair share of increasing trends spanning 60% of the total land area and dominating the land north of the 1° latitude. However, only 70% of these trends were significant at 5%. Notable trend magnitudes of 7×10^{-5} per month ranging from -5×10^{-6} to 15×10^{-5} were observed in the Luweero–Nakasongola stretch east of the Lake Albert Basin. Other areas with significantly increasing trends included West Nile, central north and northeastern Uganda, the Soroti areas in the east, and sections of Isingiro and Ntungamo in southwestern Uganda with a mean magnitude of 3×10^{-5} per month and a 95% confidence limit of -1×10^{-5} to 5×10^{-5}. However, areas within the Lake Victoria Basin, greater central region, Mt. Rwenzori, the

Kibale–Hoima stretch, the Kabarole areas of Western Uganda, Kisoro in southwestern Uganda, and Mt. Elgon regions covering over 36% of the total land area exhibited no trends. Decreasing trends existed in isolation and were cluttered over central, southern, and southwestern parts of the country.

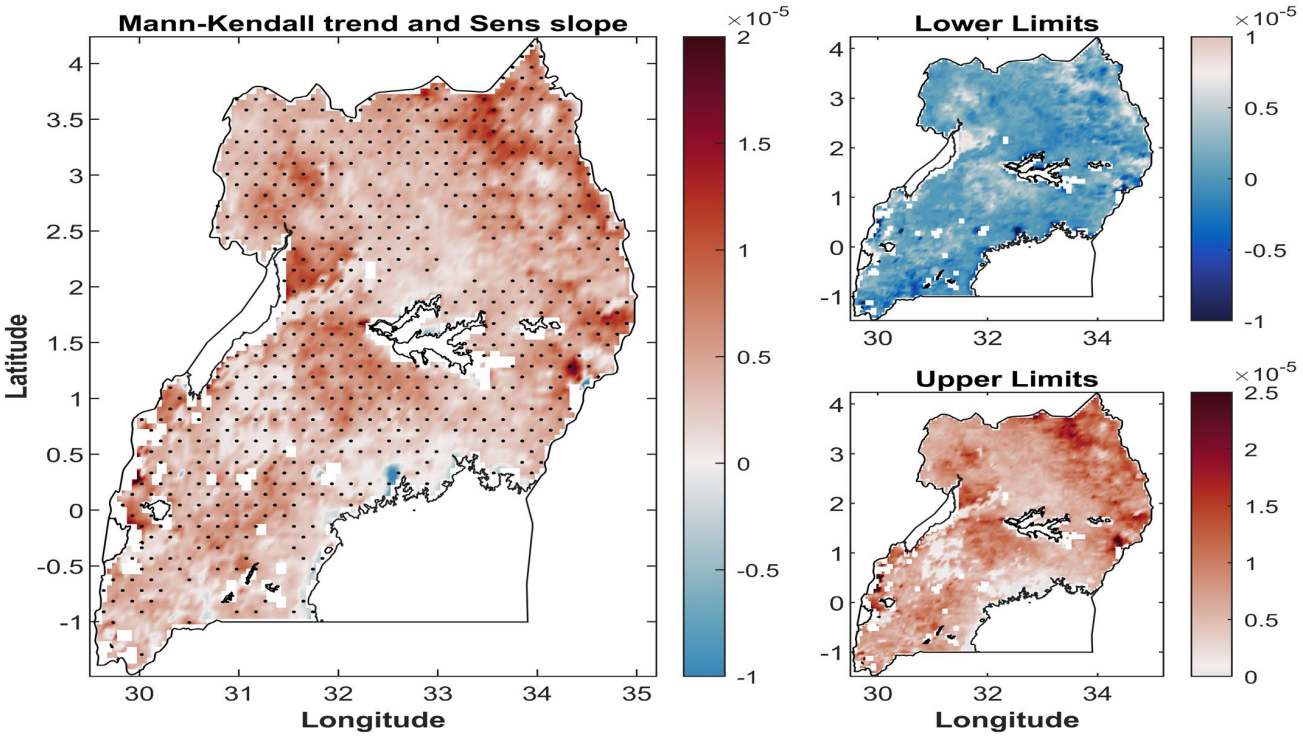

Figure 7. FAPAR trends over Uganda (1983–2013) (main plot) with 95% confidence limits (lower and upper limits, respectively). Stipples indicate significance ($p < 0.05$).

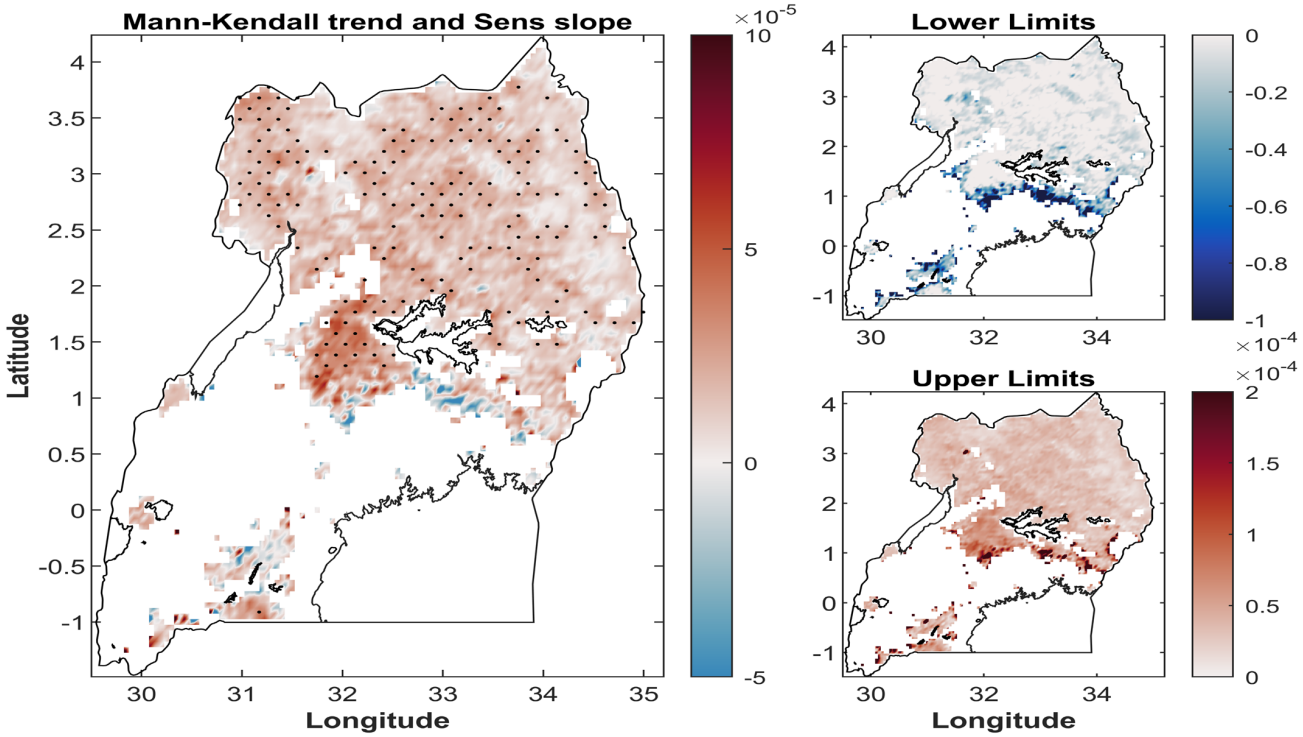

Figure 8. Trends in Standardized FAPAR Indices over Uganda (1983–2013) (main plot) with 95% confidence limits (lower and upper limits, respectively). Stipples indicate significance ($p < 0.05$).

4.3. Correlation Between Standardized FAPAR Index and Agricultural Drought Indicators

As show in Figure 9, moderate to strong positive correlations (r = 0.5–0.9) dominated the SFI and SPEI-03 relationship over Uganda, covering 80% of the total land area. The strongest correlations dominated the regions above the 1.6° latitude, with a mean *r* of 0.75 within 95% confidence limits of −0.2 and 0.9. This was followed by central Uganda with a zonal stretch from Hoima in the west, gradually decreasing towards Mbale in the east at a mean *r* of 0.5 ranging from −0.3 to 0.75. In the south, the southern districts stretching Isingiro–Mabara–Sembabule–Masaka equally had moderate positive correlations. The weakest positive correlations were scattered in the south (Rakai district), southwest (Kisoro–Kibale), and sections of western Uganda. However, no correlations were observed over sections of Mukono, Mityana, and Mubende in central Uganda, the Albert Nile stretch, Elgon slopes, Kabarole, and areas east of Lake Edward. Finally, only a negligible 3% of total land area had weak negative correlations, centered on Mt. Elgon, Kigezi highlands in the southwest, and Mt. Rwenzori region.

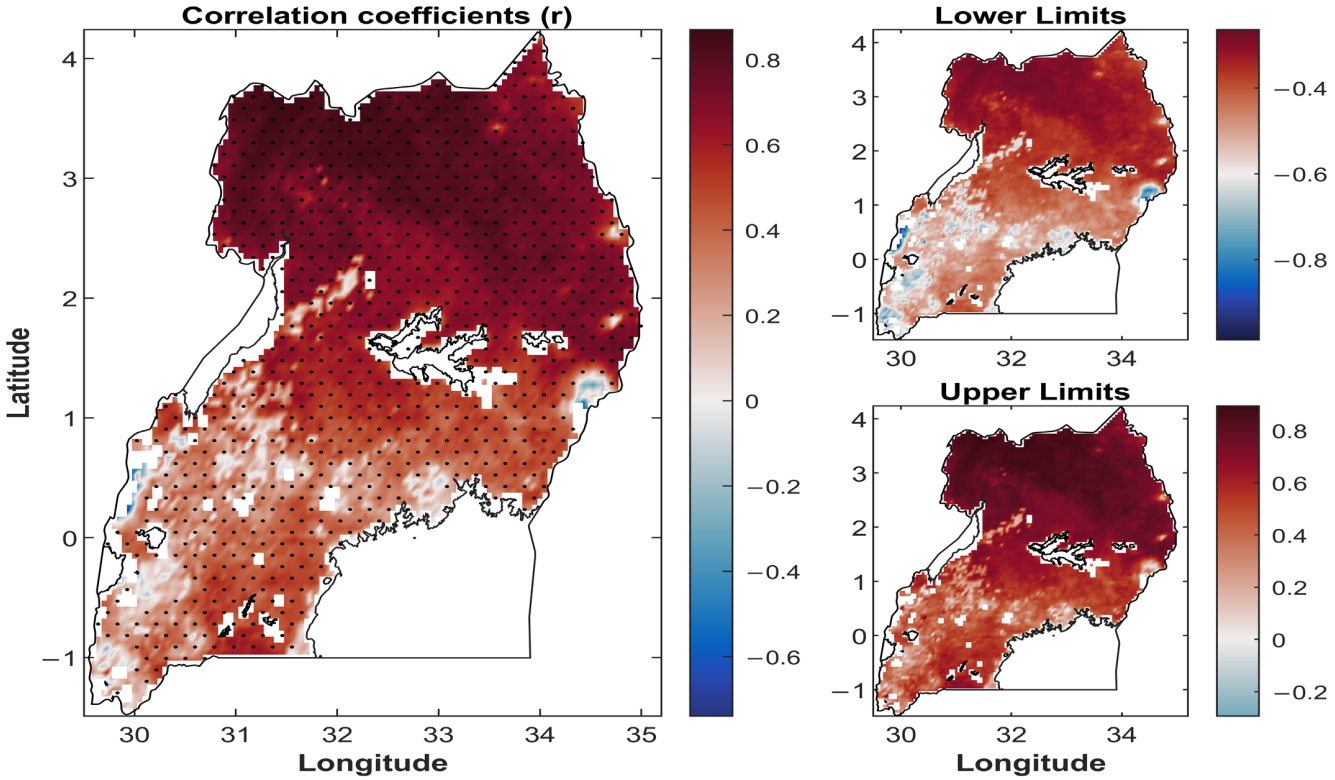

Figure 9. Correlations between SFI and SPEI-03 over Uganda (1983–2013) (main plot) with 95% confidence limits (lower and upper limits, respectively). Stipples indicate significance ($p < 0.05$).

On the other hand, as shown in Figure 10, moderate to strong negative correlations (r = 0.6–0.9) explained the relationship between SFI and CWSI over Uganda with <80% cover of the total land area. The strongest correlations were centered over central northern Uganda (Kitgum–Abim–Lira–Gulu stretch) with a westward sweep towards West Nile at a mean *r* of −0.8 within 95% confidence limits of −9 and −7. This was followed by a blend of strong–moderate negative correlations in areas of Soroti and southern Karomoja sections in the east and Hoima in the west with a mean *r* of −0.5 ranging from −0.6 to −0.45. Moderate to weak negative correlations were observed in central Uganda, greater Karamoja, and the Ankole–Masaka dry corridor in the south. However, there were no significant correlations over Mt. Elgon, Mt. Rwenzori, and the Kamwenge and Kigezi highlands in the southwest, and sections of Mukono, Mityana, and Mubende in central Uganda.

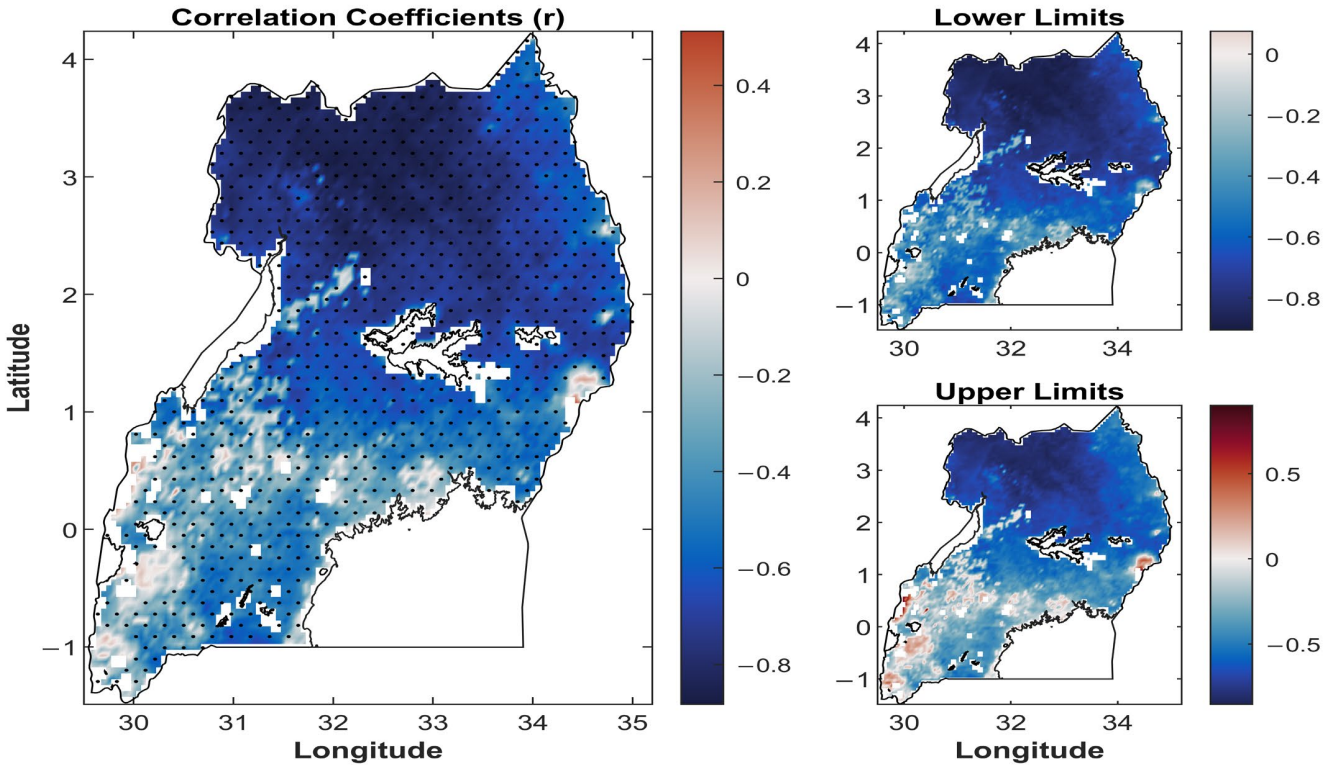

Figure 10. Correlations between SFI and CWSI over Uganda (1983–2013) (main plot) with 95% confidence limits (lower and upper limits, respectively). Stipples indicate significance ($p < 0.05$).

5. Discussions

5.1. Spatiotemporal Variability of FAPAR and FAPAR-Centered Stress Indices over Uganda

The observed spatial (climatological) patterns of photosynthetic activity over Uganda for the period 1983–2013 mimicked relief, rainfall–evapotranspiration activity, and land use patterns over the country. For example, Class 1 mimicked the highland and mountainous relief of Uganda, while the eastern sections of Classes 2 and 3 reliably reproduce the spatial patterns of monthly potential evapotranspiration over eastern Uganda [18]. Similarly, Class 4 reproduced the crop land LULC patterns over Uganda [20], whereas rainfall and convergence activity patterns over L. Victoria basin could be traced in Classes 5 and 6 [13,18].

The low values of FAPAR over the Karamoja region can be attributed to both the high evaporative demand in the region driven by high temperatures [43], skewed rainfall distribution [19] leading to prolonged water stress, and land cover dominated by wood and grassland [20] leading to low photosynthetic activity. Similarly, the observed moderate to high photosynthetic activity observed over the remaining central, western, and northern parts of the country can be attributed to reliable rainfall [19], favorable temperatures [44,45] and dominance of the croplands and forests land cover types, since these cover types have a higher carbon storage capacity and rate compared to wood and grasslands.

Likewise, the observed variations in SFI < -1 mimics vegetation and ecosystem dynamics in Uganda. For example, the observed moderate to strong deficit photosynthetic activity over the greater Karamoja region can be explained by the frequent and prevalent droughts in the region [43] suppressing LAI and vegetation cover, while the absence of major deficit anomalies over the Mukono, Wakiso, Kayunga, Luweero, Mubende, Bushenyi, Kyenjojo, Kibale, Hoima, and Masindi districts and areas in the flank of the Great Lakes during the study period explains the moderate to high performance of vegetation in these regions. This could be attributed to reliable rainfall [43] and dominance of

wetlands [20], respectively. On the other hand, the observed increasing trends in FAPAR that dominate the country can be attributed to increasing precipitation [44] over most parts of the country, major land use and land cover transformations mainly characterized by conversion of grass and woodlands to agricultural lands [46], as well as afforestation programs [20,47], increasing carbon dioxide in the atmosphere [48], and the favoring of photosynthetic activity [49–51] given FAPAR's direct role in CO_2 assimilation [52]. Conversely, the observed negative trends in FAPAR over the Kampala Metropolitan Area can be explained, according to Hackländer et al. [53], by increases in land surface temperatures owing to increasing urbanization, especially in Kampala [54] and Entebbe.

Observed increases in FAPAR-centered stress indices can be attributed to increases in both biotic and abiotic stresses that affect vegetation's ability to absorb PAR, hence indicating stress or a reduction in PAR abundance as a result of increased atmospheric albedo. For example, studies by Baron et al. [55], Bilgin et al. [56], and Vats [57] have shown the reductive effect of pests and diseases on both LAI, molecular transport, and the photochemical and metabolic capacity of vegetation. In Uganda, several studies, including Tushemereirwe et al. [58], Roux et al. [59], and recently Mulema et al. [60], have already noted increased prevalence and outbreaks of invasive pests and diseases. Similarly, abiotic stresses such as drought and soil degradation owing to climatic variation have been studied to cause stomatal closure as a response mechanism to elevated vapor pressure deficits, hence reducing CO_2 conductance and transpiration. A recent study by Magara et al. [61] using both hydrological and agrometeorological drought indices reported increases in drought magnitudes, especially over northern and northeastern parts of the country, hence partially explaining the observed trends in FAPAR-centered stresses. Likewise, a general decrease in vegetation productivity over eastern Uganda as reported Landmann and Dubovyk [62] between 2000 and 2011 can equally be cited. External drivers such as ocean–atmosphere teleconnections like ENSO can also be linked to the observed patterns [46]. However, a dedicated study on sequential and short-lived trends is recommended to expose the direct impact of ENSO and other teleconnections on vegetation photosynthetic activity.

5.2. Performance of FAPAR in Drought and Plant Water Stress Monitoring

Generally, correlation results showed a strong relationship between SFI and SPEI-03 index. This was specifically observed in areas dominated by crop and grassland. Notably, the eastern part of Karamoja was dominated by water stress for the study period and the FAPAR index was able to simulate it. These results are in agreement with similar studies by Peng et al. [12], who compared three FAPAR datasets, CGLS FAPAR, MODIS, and QA4ECV with SPEI and achieved similar positive correlations results, and Rossi et al. [63]. However, unlike the moderate to weak correlation range achieved by Peng et al. [12] owing to a lower resolution SPEI dataset [64] used their study, our study achieved stronger correlations due to the high spatial resolution of the SPEI-03 Index used.

A comparison of SFI with a direct crop water stress index (CWSI) yielded stronger negative relationships, especially in the areas dominated by cropland, grassland, and forest land cover. This implies that an increase in crop water stress over vegetated areas in Uganda could equally be a signal of vegetation activity undergoing photosynthetic stress. Intrinsically, the performance dropped significantly with little to no correlations in areas dominated by anti-floral human activities such as urbanization, deforestation, and bush burning, among others, indicating FAPAR's ability to track changes in biomass. Similarly, these results are in agreement with similar studies by Cammalleri et al. [65], Wen et al. [66], and Shahmohammadi et al.'s [67] recent study over Europe.

On the other hand, the little positive to no relationship observed between SFI and CWSI coincides with high altitude, as major zero correlation spots are located in mountainous

and high-altitude areas such Mt. Elgon, Rwenzori, Sabiny, and Muhabura as well as the Mufumbiro ranges and highlands of southwestern Uganda. This is partly so because East African mountain peaks are dominated by sparse vegetation cover [68,69] owing to harsh climatic conditions, snow, and glacial covers. The relationship could equally be explained by the fair distribution of non-photosynthetic vegetation [69,70] at high altitudes, which strongly impacts LAI [71]. However, it is recommended that a dedicated study is performed to pinpoint the source of the zero correlation in high-altitudes using stratified analysis. Nevertheless, based on the overall correlation scores, we can confidently recommend the FAPAR variable as a perfect proxy for vegetation health and water stress monitoring over Uganda.

6. Conclusions

From this study, we have shown that there are six classes of photosynthetic activity over Uganda; these are dominated by Class 4 (0.36–0.45), which covers nearly half of the total land area, spans the central, mid, north, and northwestern regions, and is associated with strong seasonal variation. The country was characterized with significant increases in monthly FAPAR and FAPAR-centered stresses (SFI < −1), covering 85% and 60% of the country, respectively. A 3-month drought indicator, SPEI-3, presented strong relationships with SFI over most parts of the country. Finally, a strong negative association was observed between SFI and the crop water stress index (CWSI), making FAPAR an ideal indicator for plant health and water stress. These results highlight the state and variation in plant health and water stress over Uganda with a holistic view on ecosystem functionality at a high spatial and temporal resolution. These results thus facilitate accurate crop conditions monitoring, predictions of crop yield, monitoring improper irrigation to inform effective agricultural planning, and drought management for resilience building. Lastly, based on the indirect validation results, we can thus recommend FAPAR, especially NOAA-AVHRR FAPAR (AVH15C1), as a robust proxy for vegetation health and water stress monitoring over Uganda. However, much emphasis should be put on the quality of the FAPAR product in use for similar applications.

Supplementary Materials: The following supporting information can be downloaded at: https://drive.google.com/file/d/1WZFqYEDiOqlZthXM-xLVSBs-eICy0Fo-/view?usp=sharing (accessed on 13 March 2025).

Author Contributions: Conceptualization, R.S. and M.V.; methodology, R.S. and M.V.; formal analysis, R.S.; investigation, R.S., A.T. and J.K.; resources, G.H.K., A.G., T.L. and G.A.; data curation, R.S.; writing—original draft preparation, R.S. and A.T.; writing—review and editing, R.S., A.T., G.H.K., T.L., J.K., A.G., G.A., Q.D. and M.V.; supervision, M.V. and G.H.K. All authors have read and agreed to the published version of the manuscript.

Funding: Dimitrie Cantemir University IR-BE-200465 project provided funding for the open access publication of this paper.

Data Availability Statement: The original contributions presented in this study are included in the Supplementary Material. Further inquiries can be directed to the corresponding author.

Acknowledgments: The first author wishes to thank the support from the European Commission through the Erasmus+ student exchange program which enabled the drafting of this paper. We also acknowledge the technical support from RCMRD-GMES Africa Project for the access and application of satellite products used in this study. We are also grateful to the anonymous reviewers for their valuable contributions that greatly improved this study.

Conflicts of Interest: Author Tuula Löytty was employed by the company Smart & Lean Hub Oy (S&L). The remaining authors declare that the research was conducted in the absence of any commercial or financial relationships that could be construed as a potential conflict of interest.

References

1. Qin, H.; Wang, C.; Zhao, K.; Xi, X. Estimation of the fraction of absorbed photosynthetically active radiation (fPAR) in maize canopies using LiDAR data and hyperspectral imagery. *PLoS ONE* **2018**, *13*, e0197510. [CrossRef]
2. Cammalleri, C.; Verger, A.; Lacaze, R.; Vogt, J.V. Harmonization of GEOV2 fAPAR time series through MODIS data for global drought monitoring. *Int. J. Appl. Earth Obs. Geoinf.* **2019**, *80*, 1–12. [CrossRef]
3. Liang, S.; Wang, J. Fraction of absorbed photosynthetically active radiation. In *Advanced Remote Sensing*, 2nd ed.; Liang, S., Wang, J., Eds.; Academic Press: Cambridge, MA, USA, 2020; pp. 447–476. [CrossRef]
4. Copernicus European Drought Observatory (EDO). *Edo Indicator Factsheet, Brussels, Belgium*; 2023; pp. 1–5. Available online: https://edo.jrc.ec.europa.eu/ (accessed on 24 September 2025).
5. Gitelson, A.A. Remote estimation of fraction of radiation absorbed by photosynthetically active vegetation: Generic algorithm for maize and soybean. *Remote Sens. Lett.* **2019**, *10*, 283–291. [CrossRef]
6. Zhang, Y.; Hu, Z.; Wang, J.; Gao, X.; Yang, C.; Yang, F.; Wu, G. Temporal upscaling of MODIS instantaneous FAPAR improves forest gross primary productivity (GPP) simulation. *Int. J. Appl. Earth Obs. Geoinf.* **2023**, *121*, 103360. [CrossRef]
7. Bayat, B.; Camacho, F.; Nickeson, J.; Cosh, M.; Bolten, J.; Vereecken, H.; Montzka, C. Toward operational validation systems for global satellite-based terrestrial essential climate variables. *Int. J. Appl. Earth Obs. Geoinf.* **2021**, *95*, 102240. [CrossRef]
8. Oyana, T.; Kayendeke, E.; Adu-Prah, S. Assessing Performance of Leaf Area Index in a Monitored Mountain Ecosystem on Mount Elgon-Uganda. *Int. J. Appl. Geospat. Res.* **2017**, *8*, 64–80. [CrossRef]
9. Gobron, N. Fraction of Absorbed Photosynthetically Active Radiation by Green Vegetation. In *Advanced Remote Sensing*; Academic Press: Cambridge, MA, USA, 2012; pp. 383–414. [CrossRef]
10. Gobron, N.; Marioni, M.; Robustelli, M.; Vermote, E. Can we use the QA4ECV black-sky fraction of absorbed photosynthetically active radiation (FAPAR) using AVHRR surface reflectance to assess terrestrial global change? *Remote Sens.* **2019**, *11*, 3055. [CrossRef]
11. Claverie, M.; Matthews, J.L.; Vermote, E.F.; Justice, C.O. A 30+ year AVHRR LAI and FAPAR climate data record: Algorithm description and validation. *Remote Sens.* **2016**, *8*, 263. [CrossRef]
12. Peng, J.; Muller, J.-P.; Blessing, S.; Giering, R.; Danne, O.; Gobron, N.; Kharbouche, S.; Ludwig, R.; Müller, B.; Leng, G.; et al. Can we use satellite-based FAPAR to detect drought? *Sensors* **2019**, *19*, 3662. [CrossRef]
13. Ssembajwe, R.; Twah, A.; Nakabugo, R.; Katende, S.; Mulinde, C.; Ddumba, S.D.; Bamutaze, Y.; Voda, M. Wind and Humidity Nexus over Uganda in the Context of Past and Future Climate Volatility. *Climate* **2025**, *13*, 86. [CrossRef]
14. Wang, N.; Jassogne, L.; van Asten, P.J.; Mukasa, D.; Wanyama, I.; Kagezi, G.; Giller, K.E. Evaluating coffee yield gaps and important biotic, abiotic, and management factors limiting coffee production in Uganda. *Eur. J. Agron.* **2015**, *63*, 1–11. [CrossRef]
15. Basalirwa, C.P.K. Delineation of Uganda into climatological rainfall zones using the method of principal component analysis. *Int. J. Climatol.* **1995**, *15*, 1161–1177. [CrossRef]
16. Mugume, I. Optimization of Numerical Models for Operational Weather. Ph.D. Thesis, Makerere University, Kampala, Uganda, 2018.
17. Stanton, M.C.; Adriko, M.; Arinaitwe, M.; Howell, A.; Davies, J.; Allison, G.; LaCourse, E.J.; Muheki, E.; Kabatereine, N.B.; Stothard, J.R. Intestinal schistosomiasis in Uganda at high altitude (>1400m): Malacological and epidemiological surveys on Mount Elgon and in Fort Portal crater lakes reveal extra preventive chemotherapy needs. *Infect. Dis. Poverty* **2017**, *6*, 26–35. [CrossRef]
18. Ssembajwe, R.; Mulinde, C.; Ddumba, S.D.; Kagezi, G.H.; Opio, R.; Kobusinge, J.; Mugagga, F.; Bamutaze, Y.; Gidudu, A.; Voda, M.; et al. Dynamics and associations of selected agrometeorological variables in Robusta growing regions of Uganda. *Agric. Water Manag.* **2025**, *307*, 109257. [CrossRef]
19. Funk, C.; Rowland, J.; Eilerts, G.; White, L. *A Climate Trend Analysis of Uganda*; Famine Early Warning Systems Network—Informing Climate Change Adaptation Series 2012–3062; U.S. Geological Survey: Reston, VA, USA, 2012; Volume Fact Sheet, pp. 1–4.
20. Karamage, F.; Zhang, C.; Liu, T.; Maganda, A.; Isabwe, A. Soil erosion risk assessment in Uganda. *Forests* **2017**, *8*, 52. [CrossRef]
21. *Land Cover Viewer: Eastern & Southern Africa*; Regional Centre For Mapping Resource For Development: Nairobi, Kenya, 2014; Land Use, Land Cover Data.
22. Abatzoglou, J.T.; Dobrowski, S.Z.; Parks, S.A.; Hegewisch, K.C. TerraClimate, a high-resolution global dataset of monthly climate and climatic water balance from 1958–2015. *Sci. Data* **2018**, *5*, 170191. [CrossRef]
23. *MATLABR2024a*, The MathWorks Inc.: Natick, MA, USA, 2019. Available online: https://www.mathworks.com (accessed on 18 May 2025).
24. Lehmann, R. 3σ-Rule for Outlier Detection from the Viewpoint of Geodetic Adjustment. *J. Surv. Eng.* **2013**, *139*, 157–165. [CrossRef]
25. Greene, C.A.; Thirumalai, K.; Kearney, K.A.; Delgado, J.M.; Schwanghart, W.; Wolfenbarger, N.S.; Thyng, K.M.; Gwyther, D.E.; Gardner, A.S.; Blankenship, D.D. The Climate Data Toolbox for MATLAB. *Geochem. Geophys. Geosyst.* **2019**, *20*, 3774–3781. [CrossRef]

26. Jones, P.W. First- and Second-Order Conservative Remapping Schemes for Grids in Spherical Coordinates. *Mon. Weather Rev.* **1999**, *127*, 2204–2210. [CrossRef]
27. Zhang, Y.; Chen, H.; Fu, S. Improvement to Patched Grid Technique with High-Order Conservative Remapping Method. *J. Aircr.* **2011**, *48*, 884–893. [CrossRef]
28. Schulzweida, U. *CDO User Guide*; Version 2.3.0; Zenodo: Geneva, Switzerland, 2023. [CrossRef]
29. Gebrehiwot, T.; van der Veen, A.; Maathuis, B. Spatial and temporal assessment of drought in the Northern highlands of Ethiopia. *Int. J. Appl. Earth Obs. Geoinf.* **2011**, *13*, 309–321. [CrossRef]
30. WMO. *Standardized Precipitation Index User Guide No. 1090*; WMO: Geneva, Switzerland, 2012.
31. Wu, W.; Li, R.; Shao, J. Assessment of Regional Spatiotemporal Variations in Drought from the Perspective of Soil Moisture in Guangxi, China. *Water* **2022**, *14*, 289. [CrossRef]
32. Vicente-Serrano, S.M.; Beguería, S.; López-Moreno, J.I. A Multiscalar Drought Index Sensitive to Global Warming: The Standardized Precipitation Evapotranspiration Index. *J. Clim.* **2010**, *23*, 1696–1718. [CrossRef]
33. Ssembajwe, R.; Nguefack, J.; Mezafack, K.L.; Kagezi, G.H.; Gidudu, A.; Arinaitwe, G.; Voda, M. Spatiotemporal dynamics and drivers of agricultural droughts in the agroecological zones of Cameroon. *Int. J. Appl. Earth Obs. Geoinf.* **2025**, *140*, 104581. [CrossRef]
34. Jackson, R.D.; Idso, S.B.; Reginato, R.J.; Pinter, P.J. Canopy temperature as a crop water stress indicator. *Water Resour. Res.* **1981**, *17*, 1133–1138. [CrossRef]
35. Adams, R.P. *K-Means Clustering and Related Algorithms*; Princeton University: Princeton, NJ, USA, 2018; pp. 1–18.
36. Yue, S.; Wang, C. The Mann-Kendall Test Modified by Effective Sample Size to Detect Trend in Serially Correlated Hydrological Series. *Water Resour. Manag.* **2004**, *18*, 201–218. [CrossRef]
37. Alashan, S. Combination of modified Mann-Kendall method and Şen innovative trend analysis. *Eng. Rep.* **2020**, *2*, e12131. [CrossRef]
38. Tabari, H.; Marofi, S.; Aeini, A.; Hosseinzadeh, P.; Mohammadi, K. Trend analysis of reference evapotranspiration in the western half of Iran. *Agric. For. Meteorol.* **2011**, *152*, 128–136. [CrossRef]
39. He, Q.; Wang, M.; Liu, K.; Li, K.; Jiang, Z. GPRChinaTemp1km: A high-resolution monthly air temperature data set for China (1951–2020) based on machine learning. *Earth Syst. Sci. Data* **2022**, *14*, 3273–3292. [CrossRef]
40. Burkey, J. *A Non-Parametric Monotonic Trend Test Computing Mann-Kendall Tau, Tau-b, and Sen's Slope Written in Mathworks-MATLAB Implemented Using Matrix Rotations*; Department of Natural Resources and Parks, Science and Technical Services section: Seattle, DC, USA, 2006. Available online: http://www.mathworks.com/matlabcentral/fileexchange/authors/23983 (accessed on 24 September 2025).
41. Welz, T.; Doebler, P.; Pauly, M. Fisher transformation based confidence intervals of correlations in fixed- and random-effects meta-analysis. *Br. J. Math. Stat. Psychol.* **2022**, *75*, 1–22. [CrossRef]
42. Mohapatra, S.; Weisshaar, J.C. Modified Pearson correlation coefficient for two-color imaging in spherocylindrical cells. *BMC Bioinform.* **2018**, *19*, 428. [CrossRef]
43. Nsubuga, F.W.; Rautenbach, H. Climate change and variability: A review of what is known and ought to be known for Uganda. *Int. J. Clim. Change Strateg. Manag.* **2018**, *10*, 752–771. [CrossRef]
44. Nsubuga, F.N.W.; Olwoch, J.M.; de Rautenbach, C.J.W.; Botai, O.J. Analysis of mid-twentieth century rainfall trends and variability over southwestern Uganda. *Theor. Appl. Climatol.* **2014**, *115*, 53–71. [CrossRef]
45. Majaliwa, J.G.M.; Tenywa, M.M.; Bamanya, D.; Majugu, W.; Isabirye, P.; Nandozi, C.; Nampijja, J.; Musinguzi, P.; Nimusiima, A.; Sridher, G.; et al. Characterization of Historical Seasonal and Annual Rainfall and Temperature Trends in Selected Climatological Homogenous Rainfall Zones of Uganda. *Glob. J. Sci. Res.* **2015**, *15*, 21–40.
46. Kalisa, W.; Igbawua, T.; Henchiri, M.; Ali, S.; Zhang, S.; Bai, Y.; Zhang, J. Assessment of climate impact on vegetation dynamics over East Africa from 1982 to 2015. *Sci. Rep.* **2019**, *9*, 16865. [CrossRef]
47. Luwa, J.K.; Bamutaze, Y.; Mwanjalolo, J.G.M.; Waiswa, D.; Pilesjö, P.; Mukengere, E.B. Impacts of land use and land cover change in response to different driving forces in Uganda: Evidence from a review. *Afr. Geogr. Rev.* **2021**, *40*, 378–394. [CrossRef]
48. Irish Aid. Uganda Climate Action Report for 2016. Resilience and Economic Inclusion Team, pp. 1–12, 2016. Available online: https://www.irishaid.ie/media/irishaidpublications/UGA-Country-Climate-Action-Reports-Uganda-2015.pdf (accessed on 25 March 2025).
49. Dusenge, M.E.; Duarte, A.G.; Way, D.A. Plant carbon metabolism and climate change: Elevated CO_2 and temperature impacts on photosynthesis, photorespiration and respiration. *New Phytol.* **2019**, *221*, 32–49. [CrossRef] [PubMed]
50. Fathurrahman, F. Effects of Carbon Dioxide Concentration on the Growth and Physiology of Albizia saman (Jacq.) Merr. *J. Ecol. Eng.* **2023**, *24*, 302–311. [CrossRef]
51. Wang, S.; Zhang, Y.; Ju, W.; Chen, J.M.; Ciais, P. Recent global decline of CO_2 fertilization effects on vegetation photosynthesis. *Science* **2020**, *370*, 1295–1300. [CrossRef]

52. Kaminski, T.; Knorr, W.; Scholze, M.; Gobron, N.; Pinty, B.; Giering, R.; Mathieu, P.P. Consistent assimilation of MERIS FAPAR and atmospheric CO_2 into a terrestrial vegetation model and interactive mission benefit analysis. *Biogeosciences* **2012**, *9*, 3173–3184. [CrossRef]
53. Hackländer, J.; Parente, L.; Ho, Y.F.; Hengl, T.; Simoes, R.; Consoli, D.; Şahin, M.; Tian, X.; Jung, M.; Wheeler, I.; et al. Land potential assessment and trend-analysis using 2000–2021 FAPAR monthly time-series at 250 m spatial resolution. *PeerJ* **2024**, *12*, e16972. [CrossRef]
54. Ogwang, J.I. Explore the Dynamics of Land-Use Changes and Its Impacts on Land Surface Temperature in Greater Kampala Metropolitan Area. Ph.D. Thesis, Makerere University, Kampala, Uganda, 2021.
55. Barón, M.; Flexas, J.; Delucia, E.H. Photosynthetic responses to biotic stress. In *Terrestrial Photosynthesis in a Changing Environment a Molecular, Physiological and Ecological Approach*; Cambridge University Press: Cambridge, UK, 2011; pp. 331–350. [CrossRef]
56. Bilgin, D.D.; Zavala, J.A.; Zhu, J.; Clough, S.J.; Ort, D.R.; Delucia, E.H. Biotic stress globally downregulates photosynthesis genes. *Plant Cell Environ.* **2010**, *33*, 1597–1613. [CrossRef] [PubMed]
57. Vats, S. *Biotic and Abiotic Stress Tolerance in Plants*; Springer: Singapore, 2018; pp. 1–367. [CrossRef]
58. Tushemereirwe, W.; Bagabe, M. Review of disease distribution and pest status in Africa. In *Mobilizing IPM for Sustainable Banana Production in Africa*; International Plant Genetic Resources Institute: Rome, Italy, 1999; pp. 139–147.
59. Roux, J.; Coutinho, T.A.; Byabashaija, D.M.; Wingfield, M.J. Diseases of plantation Eucalyptus in Uganda. *S. Afr. J. Sci.* **2001**, *97*, 16–18.
60. Mulema, J.; Nankinga, C.; Kagorora, J.P.K.; Tusiime, G.; Amayo, R.; Chemonges, M.; Gumisiriya, C.; Kato, F.; Kigongo, B.M.; Ochwo-Ssemakula, M.; et al. Prioritising non-native pest species to inform plant health biosecurity policy decisions and to safeguard agriculture, forestry, biodiversity, and livelihoods in Uganda. *Front. Agron.* **2025**, *7*, 1601845. [CrossRef]
61. Magara, G.; Okrah, A.; Yao, Y.I.S.; Yeboah, E.; Darko, G.; Akimana, D.; Awuku, V.; Quist, I.; Sarfo, I. A Quantitative Assessment of Drought Trends in Uganda Using Statistical Models for Hydrological Indicators. *Int. J. Environ. Clim. Change* **2025**, *15*, 517–537. [CrossRef]
62. Landmann, T.; Dubovyk, O. Mapping Vegetation Productivity Dynamics And Degradation Trends Over East Africa Using A Decade Of Medium Resolution Modis Time-Series Data. In Proceedings of the 2013 IEEE International Geoscience and Remote Sensing Symposium-IGARSS, Melbourne, Australia, 21–26 July 2013; pp. 1801–1804.
63. Rossi, S.; Weissteiner, C.; Laguardia, G.; Kurnik, B.; Robustelli, M.; Niemeyer, S.; Gobron, N. Potential of MERIS fAPAR for drought detection. In Proceedings of the 2nd MERIS/(A)ATSR User Workshop, Frascati, Italy, 22–26 September 2008; Volume 2008.
64. Beguería, S.; Vicente-Serrano, S.M.; Reig, F.; Latorre, B. Standardized precipitation evapotranspiration index (SPEI) revisited: Parameter fitting, evapotranspiration models, tools, datasets and drought monitoring. *Int. J. Climatol.* **2014**, *34*, 3001–3023. [CrossRef]
65. Cammalleri, C.; McCormick, N.; Toreti, A. Analysis of the relationship between yield in cereals and remotely sensed fAPAR in the framework of monitoring drought impacts in Europe. *Nat. Hazards Earth Syst. Sci.* **2022**, *22*, 3737–3750. [CrossRef]
66. Wen, W.; Timmermans, J.; Chen, Q.; Van Bodegom, P.M. Monitoring the combined effects of drought and salinity stress on crops using remote sensing in the Netherlands. *Hydrol. Earth Syst. Sci.* **2022**, *26*, 4537–4552. [CrossRef]
67. Shahmohammadi, A.; Rolle, M.; Tamea, S. Vegetation Indices for plant water stress detection from satellite imagery. In *Return Dissemination Workshop 1–2 February*; Zenodo: Geneva, Switzerland, 2024; pp. 73–75. [CrossRef]
68. Hedberg, O. Altitudinal zonation of the vegetation on the east african mountains. *Proc. Linn. Soc. Lond.* **1955**, *165*, 134–136. [CrossRef]
69. Soto, G.E.; Wilcox, S.W.; Clark, P.E.; Fava, F.P.; Jensen, N.D. Mapping rangeland health indicators in eastern Africa from 2000 to 2022. *Earth Syst. Sci. Data* **2024**, *16*, 5375–5404. [CrossRef]
70. Verrelst, J.; Halabuk, A.; Atzberger, C.; Hank, T.; Steinhauser, S.; Berger, K. A comprehensive survey on quantifying non-photosynthetic vegetation cover and biomass from imaging spectroscopy. *Ecol. Indic.* **2023**, *155*, 110911. [CrossRef]
71. Xu, D.; An, D.; Guo, X. The Impact of Non-Photosynthetic Vegetation on LAI Estimation by NDVI in Mixed Grassland. *Remote Sens.* **2020**, *12*, 1979. [CrossRef]

Disclaimer/Publisher's Note: The statements, opinions and data contained in all publications are solely those of the individual author(s) and contributor(s) and not of MDPI and/or the editor(s). MDPI and/or the editor(s) disclaim responsibility for any injury to people or property resulting from any ideas, methods, instructions or products referred to in the content.